

Signal-Adapted Decomposition of Graph Signals

Harry H. Behjat^{1,2,✉}, Carl-Fredrik Westin³, Rik Ossenkoppele^{1,4}, and Dimitri Van De Ville^{5,6}

¹Department of Clinical Sciences Malmö, Lund University, Lund, Sweden

²Department of Biomedical Engineering, Lund University, Lund, Sweden

³Department of Radiology, Brigham and Women's Hospital, Harvard Medical School, Boston, Massachusetts, USA

⁴VU University Medical Center, Amsterdam UMC, Amsterdam, Netherlands

⁵Neuro-X Institute, Ecole Polytechnique Federale de Lausanne, Lausanne, Switzerland

⁶Department of Radiology and Medical Informatics, University of Geneva, Geneva, Switzerland

*✉ Corresponding author; e-mail: harry.behjat@gmail.com

Analysis of signals defined on complex topologies modeled by graphs is a topic of increasing interest. Signal decomposition plays a crucial role in the representation and processing of such information, in particular, to process graph signals based on notions of scale (e.g., coarse to fine). The graph spectrum is more irregular than for conventional domains; i.e., it is influenced by graph topology, and, therefore, assumptions about spectral representations of graph signals are not easy to make. Here, we propose a tight frame design that is adapted to the graph Laplacian spectral content of given classes of graph signals. The design is based on using the ensemble energy spectral density, a notion of spectral content of given signal sets that we determine either directly using the graph Fourier transform or indirectly through a polynomial-based approximation scheme. The approximation scheme has the benefit that (i) it does not require eigendecomposition of the Laplacian matrix making the method feasible for large graphs, and (ii) it leads to a smooth estimate of the spectral content. A prototype system of spectral kernels each capturing an equal amount of energy is initially defined and subsequently warped using the signal set's ensemble energy spectral density such that the resulting subbands each capture an equal amount of ensemble energy. This approach accounts at the same time for graph topology and signal features, and it provides a meaningful interpretation of subbands in terms of coarse-to-fine representations. We also show how more simplified designs of signal-adapted decomposition of graph signals can be adopted based on ensemble energy estimates. We show the application of proposed methods on the Minnesota road graph and three different designs of brain graphs derived from neuroimaging data.

1. Introduction

Many fields of science rely on network analysis to study complex systems. Networks are modeled mathematically as weighted graphs that have a set of nodes (vertices) with interactions between them represented by connections (links) and associated strengths. A rich repertoire of methods have been developed to pursue original queries and integrate the complexity of network structure into the analysis, subsequently providing new interpretations of datasets in divers scientific disciplines ranging from social sciences to physics and biology. One of the successes in network analysis is the ability to identify sets of nodes based on their connectivity. Traditional graph partitioning goes back to optimizing graph cuts (Fiedler,

1973), while more recent community detection identifies sets of nodes that are more densely connected inside the set than outside (Girvan and Newman, 2002). Community detection has been widely applied and many variants of the corresponding optimization criterion have been proposed (Newman, 2010).

Another major trend is the emergence of methods for processing data that reside on top of networks (Ortega et al., 2018; Shuman et al., 2013; Sandryhaila and Moura, 2013; Stankovic et al., 2019). Measurements on a network's nodes can be viewed as graph signals, enabling the extension of classical signal processing operations such as denoising, filtering, and transformation by leveraging the network's underlying connectivity. Numerous approaches have been proposed to generalize multiresolution transforms, filter bank designs, and dictionary constructions to the graph domain. These studies fall primarily into two categories: spatial (vertex) and spectral (frequency) designs. Schemes that fall within the former family include methods for designing wavelets for hierarchical trees (Ram et al., 2012; Gavish et al., 2010) and methods based on lifting schemes (Jansen et al., 2009; Narang and Ortega, 2009). The latter family is based on spectral graph theory (Chung, 1997), which is a powerful approach based on the eigendecomposition of matrices associated with graphs such as the adjacency matrix or graph Laplacian. Its strength lies in the global nature of eigenvectors, which capture key graph properties and enable solutions to convex relaxations of graph cut minimization (Von Luxburg, 2007), or to define signal-processing operations by a graph equivalent of the Fourier transform (Shuman et al., 2013). In its application to graph signal processing, operations are performed in the spectral domain using graph spectral filters. One of the first proposals, the spectral graph wavelet transform (SGWT) frame (Hammond et al., 2011), is built using scaled cubic spline spectral kernels and a low-pass spectral polynomial kernel. Moreover, various constructions of systems of spectral graph kernels leading to tight frames were proposed in (Leonardi and Van De Ville, 2013; Shuman, 2020; Isufi et al., 2024). Tight frames are particularly interesting because of their property of energy conservation between the original and transformed domain (Benedetto and Fickus, 2003). Other approaches to spectral domain design include diffusion wavelets (Coifman and Maggioni, 2006), vertex-frequency frames (Shuman et al., 2015; Stankovic et al., 2017; Ghandehari

et al., 2021; Stanković et al., 2020) and approaches to graph filter-bank design using bipartite graph decompositions (Narang and Ortega, 2012; Tanaka and Sakiyama, 2014; Zhao and Tay, 2023), connected sub-graph decomposition (Tremblay and Borgnat, 2016), graph coloring (Shuman et al., 2016) and Slepian functions that provide a trade-off between temporal and spectral energy concentration (Van De Ville et al., 2017).

A key challenge of the graph spectrum is its dependence on the graph itself, making the spectral representation of a graph signal reliant on both the domain and the signal. However, most spectral designs define spectral windows independently of the graph and signal. The first major methodology that employed adaptation to the graph's spectral properties is the spectrum-adapted tight graph wavelet and vertex-frequency frames proposed in (Shuman et al., 2015). These kernels address the non-uniform distribution of Laplacian eigenvalues, ensuring each spectral kernel supports a similar number of eigenvalues. In (Thanou et al., 2014; Yankelevsky and Elad, 2016), numerical dictionary learning approaches were proposed, where dictionaries are learned from training signals. These learned kernels are indirectly adapted to both the graph Laplacian spectrum and the training data by incorporating the graph structure into the learning process. An application-specific approach in (Behjat et al., 2015) tailored the Meyer-like frame design (Leonardi and Van De Ville, 2013) to the spectral content of functional MRI signals, producing narrow-support kernels covering the lower end of the spectrum. Here we propose an approach for constructing tight graph frames that incorporate both the intrinsic graph topology, as in (Shuman et al., 2015), and the characteristics of a given signal set. This is achieved by considering a graph-based energy spectral density notion that includes signal and topology properties and encodes the energy-wise significance of the graph eigenvalues. A system of spectral kernels tailored to the energy spectral density is constructed by starting from the design of a prototype tight frame with uniform spectral coverage, followed by a warping step which incorporates the energy spectral density information to the prototype design, resulting in a tight frame with equi-energy subbands. We also present results of more simplified designs tight frames that are adapted to the signal energy content of signal sets at hand, without the explicit need to incorporate the warping step.

2. Preliminaries

2.A. Graphs and Spectral Graph Theory

A graph can be denoted as $G = (V, E)$ with N_g vertices in set V , a set of edges as tuples (i, j) in E where $i, j \in V$. The size of the graph is the number of vertices. In this work, we only consider undirected graphs without self-loops. Algebraically, G can be represented with the node-to-node adjacency matrix A , with elements $a_{i,j}$ denoting the weight of the edge (i, j) if $(i, j) \in E$; $a_{i,j} = 0$ if $(i, j) \notin E$. The degree matrix D of G is diagonal with el-

ements $d_{i,i} = \sum_j a_{i,j}$. The Laplacian matrices of G in combinatorial form L and normalized form \mathcal{L} are defined as

$$L = D - A, \quad (1)$$

$$\mathcal{L} = D^{-1/2} L D^{-1/2}, \quad (2)$$

respectively. Both L and \mathcal{L} are symmetric and positive semi-definite, and thus, their diagonalizations lead to a set of N_g real, non-negative eigenvalues that define the graph Laplacian spectrum

$$\Lambda(G) = \{0 = \lambda_1 \leq \lambda_2 \leq \dots \leq \lambda_{N_g} = \lambda_{\max}\}. \quad (3)$$

The corresponding set of eigenvectors $\{\vec{\chi}_l\}_{l=1}^{N_g}$ forms a complete set of orthonormal vectors that span the graph spectral domain (Chung, 1997). When necessary, we use the notations $\Lambda_L(G)$ and $\Lambda_{\mathcal{L}}(G)$ to distinguish between the two definitions of the graph Laplacian. As the eigenvalues may be repetitive, for each λ_l , we denote its algebraic multiplicity by m_{λ_l} and the index of its first occurrence by i_{λ_l} . That is, if λ_l is singular, i.e. $m_{\lambda_l} = 1$, then $i_{\lambda_l} = l$, and if λ_l is repetitive, then $i_{\lambda_l} \leq l$. The multiplicity of eigenvalues equal to zero reflects the number of connected components in the graph. In this paper, only connected graphs are considered, and thus, $m_{\lambda_1} = 1$.

2.B. Graph Signals: Vertex versus Spectral Representations

Let $\ell_2(G)$ denote the Hilbert space of all square-summable real-valued vectors $\vec{f} \in \mathbb{R}^{N_g}$, with the inner product defined as

$$\langle \vec{f}_1, \vec{f}_2 \rangle = \sum_{n=1}^{N_g} f_1[n] f_2[n], \quad \forall \vec{f}_1, \vec{f}_2 \in \ell_2(G) \quad (4)$$

and the norm as

$$\|\vec{f}\|_2^2 = \langle \vec{f}, \vec{f} \rangle = \sum_{n=1}^{N_g} |f[n]|^2, \quad \forall \vec{f} \in \ell_2(G). \quad (5)$$

A real signal defined on the vertices of a graph, $f: V \rightarrow \mathbb{R}$, can be seen as a vector in $\ell_2(G)$, where the n -th element represents the value of the signal on the n -th vertex. For any $\vec{f} \in \ell_2(G)$, its spectral representation $\hat{\vec{f}} \in \ell_2(G)$, known as the graph Fourier transform of \vec{f} , can be used to express \vec{f} in terms of the graph Laplacian eigenvectors

$$f[n] = \sum_{l=1}^{N_g} \underbrace{\langle \vec{f}, \vec{\chi}_l \rangle}_{=f[l]} \chi_l[n]. \quad (6)$$

With this definition of the Fourier transform, it can be shown that the Parseval relation holds (Shuman et al., 2015)

$$\forall \vec{f}_1, \vec{f}_2 \in \ell_2(G), \quad \langle \vec{f}_1, \vec{f}_2 \rangle = \langle \hat{\vec{f}}_1, \hat{\vec{f}}_2 \rangle. \quad (7)$$

2.C. Filtering of Graph Signals

In the graph setting, the generalized convolution product is defined as

$$(\vec{f}_1 * \vec{f}_2)[n] = \sum_{l=1}^{N_g} \hat{f}_1[l] \hat{f}_2[l] \chi_l[n], \quad \forall \vec{f}_1, \vec{f}_2 \in \ell_2(G). \quad (8)$$

In analogy with conventional signal processing, filtering of graph signals can be viewed as an operation in the spectral domain. For a given graph signal $\vec{f} \in \ell_2(G)$ and graph filter $\vec{g} \in \ell_2(G)$, defined through its Fourier transform $\hat{\vec{g}}$, the filtered signal, denoted by $(F_{\vec{g}}\vec{f})$, can be obtained as

$$(F_{\vec{g}}\vec{f})[n] = (\vec{g} * \vec{f})[n] \quad (9)$$

$$\stackrel{(8)}{=} \sum_{l=1}^{N_g} \hat{g}[l] \hat{f}[l] \chi_l[n]. \quad (10)$$

For the graph filter \vec{g} , the filter response of an impulse at vertex m

$$\vec{f} = \vec{\delta}_m \leftrightarrow \hat{\delta}_m[l] = \langle \vec{\delta}_m, \vec{\chi}_l \rangle = \chi_l[m], \quad (11)$$

can be obtained as

$$(F_{\vec{g}}\vec{\delta}_m)[n] = \sum_{l=1}^{N_g} \hat{g}[l] \chi_l[m] \chi_l[n]. \quad (12)$$

The impulse response of a graph filter is, in general, shift-variant; i.e., the impulse response at one vertex is not simply a shifted version of the impulse response at any other node. This is due to the absence of a well-defined shift operator in the graph setting as that defined in the Euclidean setting. Therefore, a graph filter is conventionally defined by its spectral kernel $\hat{\vec{g}}$ rather than by its impulse response.

Although the graph spectrum is discrete, to design spectral kernels, it is often more elegant to define an underlying smooth continuous kernel. Let $L_2(G)$ denote the Hilbert space of all square-integrable spectral functions $K(\lambda) : [0, \lambda_{\max}] \rightarrow \mathbb{R}^+$, with the inner product defined as

$$\langle K_1, K_2 \rangle_{L_2} = \int_{-\infty}^{+\infty} K_1(\lambda) K_2(\lambda) d\lambda, \quad \forall K_1, K_2 \in L_2(G), \quad (13)$$

and the L_2 -norm defined as

$$\|K\|_{L_2}^2 = \langle K, K \rangle_{L_2}, \quad \forall K \in L_2(G). \quad (14)$$

A discrete version of $K(\lambda) \in L_2(G)$ can then be determined as

$$k[l] = K(\lambda_l), \quad l = 1, \dots, N_g. \quad (15)$$

Note that although \vec{k} is defined in the spectral domain, it is not linked to any explicit vertex representation, and thus, the Fourier symbol $\hat{\cdot}$ is not used for their denotation. This notation convention will be used throughout the paper.

2.D. Dictionary of Graph Atoms

For a given spectral kernel \vec{k} associated with $K(\lambda)$, the vertex-domain impulse responses are obtained as

$$\vec{\psi}_{K,m} = (F_{\vec{k}}\vec{\delta}_m) \leftrightarrow \hat{\psi}_{K,m}[l] = k[l] \chi_l[m]. \quad (16)$$

The collection of impulse responses $\{\vec{\psi}_{K,m}\}_{m=1}^{N_g}$ are considered as graph *atoms* associated with spectral kernel $K(\lambda)$. Given a set of J spectral kernels $\{\vec{k}_j \in \ell_2(G)\}_{j=1}^J$, a dictionary of graph atoms D_G with JN_g elements can be obtained

$$D_G = \left\{ \{\vec{\psi}_{K_j,m}\}_{j=1}^J \right\}_{m=1}^{N_g}. \quad (17)$$

The atoms of D_G form a frame in $\ell_2(G)$ if there exist bounds $B_2 \geq B_1 > 0$ such that (Benedetto and Fickus, 2003)

$$\forall \vec{f} \in \ell_2(G), \quad B_1 \|\vec{f}\|_2^2 \leq \sum_{j,m} |\langle \vec{f}, \vec{\psi}_{K_j,m} \rangle|^2 \leq B_2 \|\vec{f}\|_2^2, \quad (18)$$

where the frame bounds are given by

$$B_1 = \min_{\lambda \in [0, \lambda_{\max}]} G(\lambda), \quad B_2 = \max_{\lambda \in [0, \lambda_{\max}]} G(\lambda), \quad (19)$$

and $G(\lambda) \in L_2(G)$ is defined as

$$G(\lambda) = \sum_{j=1}^J |K_j(\lambda)|^2. \quad (20)$$

In particular, D_G forms a tight frame if

$$\forall \lambda \in [0, \lambda_{\max}], \quad G(\lambda) = C, \quad (21)$$

and a Parseval frame if $C = 1$.

2.E. Decomposition of Graph Signals

Direct Decomposition. To decompose a graph signal \vec{f} onto a set of the atoms in D_G , the coefficients can be obtained as

$$c_{K_j,m} = \langle \vec{f}, \vec{\psi}_{K_j,m} \rangle \quad (22)$$

$$\stackrel{(7)}{=} \sum_{l=1}^{N_g} \hat{\psi}_{K_j,m}[l] \hat{f}[l], \quad (23)$$

$$\stackrel{(16)}{=} \sum_{l=1}^{N_g} k_j[l] \hat{f}[l] \chi_l[m]. \quad (24)$$

Relation (24) shows that the direct decomposition requires a full eigendecomposition of the L since it requires i) the Laplacian eigenvectors $\{\vec{\chi}_l\}_{l=1}^{N_g}$ and ii) the graph Fourier transform of the signal $\hat{\vec{f}}$.

If D_G forms a Parseval frame, the coefficients can be used

to recover the original signal as

$$\begin{aligned}
f[n] &= \sum_j \sum_m c_{K_j, m} \vec{\psi}_{K_j, m} \\
&= \sum_j \sum_m \sum_l k_j[l] \hat{f}[l] \chi_l[m] \sum_{l'} k_j[l'] \vec{\chi}_{l'}[m] \chi_{l'}[n] \\
&= \sum_l \sum_{l'} \sum_j k_j[l] k_j[l'] \hat{f}[l] \chi_{l'}[n] \underbrace{\sum_m \chi_l[m] \chi_{l'}[m]}_{\delta_{l-l'}} \\
&= \sum_l \underbrace{\sum_j k_j^2[l]}_{=1} \hat{f}[l] \chi_l[n]. \tag{25}
\end{aligned}$$

Decomposition Through Polynomial Approximation. The decomposition of \vec{f} on D_G leads to a coefficient vector associated to each k_j given as

$$\vec{c}_{K_j} = [c_{K_j, 1}, c_{K_j, 2}, \dots, c_{K_j, N_g}]^T \tag{26}$$

$$\stackrel{(24)}{=} \sum_{l=1}^{N_g} k_j[l] \hat{f}[l] \vec{\chi}_l, \tag{27}$$

that can be interpreted as filtered versions of \vec{f} with different spectral kernels $\{k_j\}_{j=1}^J$. Due to the redundancy of such a transform, it is beneficial to implement the transform using a fast algorithm, rather than using the explicit computation of the coefficients through (24). Moreover, for large graphs, it can be cumbersome to compute the full eigendecomposition of L , and in extensively large graphs—unless for graphs of special form e.g. those that have structures similar to graphons (Ghandehari et al., 2022)—this can in fact be impossible. One solution to overcome this computational burden is to use a polynomial approximation scheme.

One such algorithm is the truncated Chebyshev polynomial approximation method (Hammond et al., 2011), which is based on considering the expansion of the continuous spectral window functions $\{K_j(\lambda)\}_{j=1}^J$ with the Chebyshev polynomials $C_p(x) = \cos(p \arccos(x))$ as

$$K_j(\lambda) = \frac{1}{2} d_{K_j, 0} + \sum_{p=1}^{\infty} d_{K_j, p} \bar{C}_p(\lambda), \tag{28}$$

where $\bar{C}_p(x) = C_p(\frac{x-b}{b})$, $b = \lambda_{\max}/2$ and $d_{K_j, p}$ denote the Chebyshev coefficients obtained as

$$d_{K_j, p} = \frac{2}{\pi} \int_0^{\pi} \cos(p\theta) K_j(b(\cos(\theta) + 1)) d\theta. \tag{29}$$

By truncating (28) to M terms, $K_j(\lambda)$ can be approximated as an M -th order polynomial $P_j(\lambda) \in L_2(G)$. Con-

sequently, \vec{c}_{K_j} can be approximated as

$$\vec{c}_{K_j} \stackrel{(27)}{=} \sum_{l=1}^{N_g} \underbrace{k_j[l]}_{K_j(\lambda_l)} \hat{f}[l] \vec{\chi}_l \tag{30}$$

$$\approx \sum_{l=1}^{N_g} P_j(\lambda_l) \hat{f}[l] \vec{\chi}_l \tag{31}$$

$$= P_j(L) \sum_{l=1}^{N_g} \hat{f}[l] \vec{\chi}_l \tag{32}$$

$$\stackrel{(6)}{=} P_j(L) \vec{f} \tag{33}$$

where in (32) we exploit the property $L\chi_l = \lambda_l\chi_l \Rightarrow P_j(L)\chi_l = P_j(\lambda_l)\chi_l$.

3. Spectral Warping

Given a spectral kernel $K(\lambda) \in L_2(G)$ and a function $T_F(\lambda) \in L_2(G) : [0, \lambda_{\max}] \rightarrow [0, \lambda_{\max}]$, $K(\lambda)$ can be warped using $T_F(\lambda)$ as $K'(\lambda) = K(T_F(\lambda))$. The resulting kernel $K'(\lambda)$ remains a kernel $\in L_2(G)$ and also satisfies $\|K(T_F(\lambda))\|_{L_2} = \|K\|_{L_2}$.

More generally, given a system of spectral kernels $\{K_j(\lambda)\}_{j=1}^J$ that form a tight frame, spectral warping using $T_F(\lambda)$ results in a warped system of kernels which retain the tight frame property, i.e. (19)-(21) for the same frame bounds as in the original system of kernels, since:

$$\begin{aligned}
\sum_{j=1}^J |K'_j(\lambda)|^2 &= \sum_{j=1}^J |K_j(\underbrace{T_F(\lambda)}_{:=\lambda'})|^2, \quad \forall \lambda \in [0, \lambda_{\max}] \\
&= \sum_{j=1}^J |K_j(\lambda')|^2, \quad \forall \lambda' \in [0, \lambda_{\max}].
\end{aligned}$$

4. Prototype Systems of Spectral Kernels

There are a number of prototype systems of spectral kernels that can be leveraged in different stages of performing signal-adapted decomposition of graph signals. In particular, there are two stages that systems of spectral kernels are used: (i) to estimate the energy spectral density of a graph signal; (ii) to decompose a graph signal. For (i), generally a system with a large number of kernels is desired to obtain a suitable and sufficiently detailed estimate of the distribution of signal energy across the graph spectrum. For (ii), generally a small number of kernels is desired to characterise the signal at multiple interpretable spectral subbands. In the following, the construction detail and properties of two different categories of kernels are given, the first of which is used for (i) and the second one is used for (ii).

4.A. B-spline based System of Spectral Kernels

The central B-spline of degree n , denoted $\beta^{(n)}(x)$, is a compactly-supported function in the interval

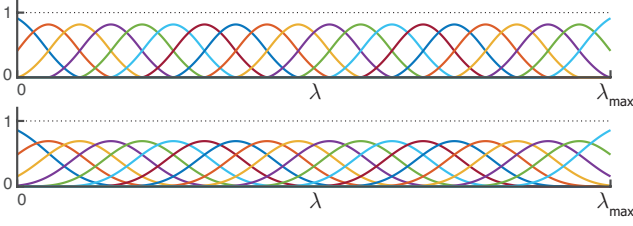


Figure 1. B-spline based system of spectral kernels with 20 spectral bands constructed based on B-splines of order 3 (top) and 7 (bottom). The dotted lines correspond to $G(\lambda)$ in (20), i.e., property (38).

$[-\Delta^{(n)}, \Delta^{(n)}]$, i.e., $\beta^{(n)}(x) = 0$ for all $|x| \geq \Delta^{(n)}$ where $\Delta^{(n)} = (n+1)/2$, and is obtained through the $(n+1)$ -fold convolution as

$$\beta^{(n)}(x) = \underbrace{\beta^{(0)}(x) * \beta^{(0)}(x) * \dots * \beta^{(0)}(x)}_{(n+1)\text{times}}, \quad (34)$$

where

$$\beta^{(0)}(x) = \begin{cases} 1, & -\frac{1}{2} < x < \frac{1}{2} \\ \frac{1}{2}, & |x| = \frac{1}{2} \\ 0, & \text{otherwise.} \end{cases} \quad (35)$$

Proposition 1: (B-spline based Parseval Frame on Graphs) For a given graph G and B-spline generating function $\beta^{(n)}(x)$, $n \geq 2$, a set of B-spline based spectral kernels $\{B_j(\lambda) \in L_2(G)\}_{j=1}^J$ can be defined as

$$B_j(\lambda) = \begin{cases} \tilde{B}_j(\lambda) + \sum_{i=-\Delta}^0 \tilde{B}_i(\lambda), & j = 1 \\ \tilde{B}_j(\lambda), & j = 2, \dots, J-1 \\ \tilde{B}_j(\lambda) + \sum_{i=J+\Delta+1}^J \tilde{B}_i(\lambda), & j = J \end{cases} \quad (36)$$

where $\Delta = \lfloor n/2 \rfloor - 1$ and $\tilde{B}_i(\lambda) \in L_2(G)$ is defined as

$$\tilde{B}_i(\lambda) = \sqrt{\beta^{(n)}\left(\frac{\lambda_{\max}}{J-1}(\lambda - l + 1)\right)}, \quad l = -\Delta, \dots, J + \Delta + 1. \quad (37)$$

The system of kernels $\{B_j(\lambda)\}_{j=1}^J$ satisfy

$$\sum_{j=1}^J |B_j(\lambda)|^2 = 1, \quad \forall \lambda \in [0, \lambda_{\max}], \quad (38)$$

and, thus, their associated dictionary of atoms forms a Parseval frame.

Proof: See Appendix I. ■

Fig. 1 shows two realizations of B-spline based systems of spectral kernels. The systems entail wide, overlapping passband kernels. Moreover, the kernels are smooth, which enables their seamless approximation as low order polynomials.

The system of kernels defined in Proposition 1 are uniformly spread across the spectrum. Such a system is suitable to estimate the overall of distribution of energy of graph signals across the spectrum. However, given that real-world graph signals are generally lowpass, it can be efficient to leverage a larger number of kernels at the lower-end of the spectrum to enable a more

fine-scale estimation of the low-frequency energy content. To this aim, the uniform system of kernels given in Proposition 1 can be tailored to entail a multiresolution characteristic, wherein the lower-end kernels become more narrow-band passband up to a desired pivot point— $\lambda^{(\text{piv})} \in (0, \lambda_{\max})$, $\lambda^{(\text{piv})} \ll \lambda_{\max}$ —in the spectrum after which the kernels become more wide-band passband kernels. This can be done by defining a piecewise linear warping function as

$$P(\lambda) = \begin{cases} m_1 \lambda, & 0 \leq \lambda \leq \lambda^{(\text{piv})}, \\ m_2(\lambda - \lambda^{(\text{piv})}) + y^{(\text{piv})}, & \lambda^{(\text{piv})} < \lambda \leq \lambda_{\max}, \end{cases} \quad (39)$$

where $m_1 = y^{(\text{piv})}/\lambda^{(\text{piv})}$ and $m_2 = (1 - y^{(\text{piv})})/(\lambda_{\max} - \lambda^{(\text{piv})})$ are line slopes, $y^{(\text{piv})} = N_{\text{lower}}/N_{\text{total}}$, and N_{lower} and N_{total} are the number of kernels that are to cover the lower-end of the spectrum and the entire spectrum, respectively. Smoothing $P(\lambda)$ eliminates the sharp transition between its piecewise linear components, yielding a well-behaved warping function. This ensures a smooth system of warped kernels, enabling practical polynomial approximations for signal decomposition, cf. E. Fig. 2 shows a multiresolution system of B-spline based kernels obtained by warping the uniformly distributed system of B-spline based kernels in Proposition 1, with $N_{\text{total}} = 57$, using a smoothed version of $P(\lambda)$.

4.B. Meyer-like Uniform System of Spectral Kernels

Proposition 2: (uniform Meyer-type (UMT) system of spectral kernels) Using the auxiliary function of the Meyer wavelet, given by (Meyer, 1986)

$$\nu(x) = x^4(35 - 84x + 70x^2 - 20x^3), \quad (40)$$

a set of $J \geq 2$ spectral kernels defined as

$$U_1(\lambda) = \begin{cases} 1 & \forall \lambda \in [0, a] \\ \cos(\frac{\pi}{2}\nu(\frac{1}{\gamma-1}(\frac{\lambda}{a} - 1))) & \forall \lambda \in [a, \gamma a] \\ 0 & \text{elsewhere} \end{cases} \quad (41a)$$

$$U_j(\lambda) = \begin{cases} \sin(\frac{\pi}{2}\nu(\frac{1}{\gamma-1}(\frac{\lambda - (j-2)\Delta}{a} - 1))) & \forall \lambda \in]\lambda_I, \lambda_{II}] \\ \cos(\frac{\pi}{2}\nu(\frac{1}{\gamma-1}(\frac{\lambda - (j-1)\Delta}{a} - 1))) & \forall \lambda \in]\lambda_{II}, \lambda_{II} + \Delta] \\ 0 & \text{elsewhere} \end{cases} \quad (41b)$$

$$U_J(\lambda) = \begin{cases} \sin(\frac{\pi}{2}\nu(\frac{1}{\gamma-1}(\frac{\lambda - (J-2)\Delta}{a} - 1))) & \forall \lambda \in]\lambda_I, \lambda_{II}] \\ 1 & \forall \lambda \in]\lambda_{II}, \lambda_{II} + a] \\ 0 & \text{elsewhere} \end{cases} \quad (41c)$$

can be constructed, where

$$\Delta = \gamma a - a, \quad (42a)$$

$$\lambda_I = a + (j-2)\Delta, \quad (42b)$$

$$\lambda_{II} = \gamma a + (j-2)\Delta, \quad (42c)$$

$$a = \frac{\lambda_{\max}}{J\gamma - J - \gamma + 3}. \quad (42d)$$

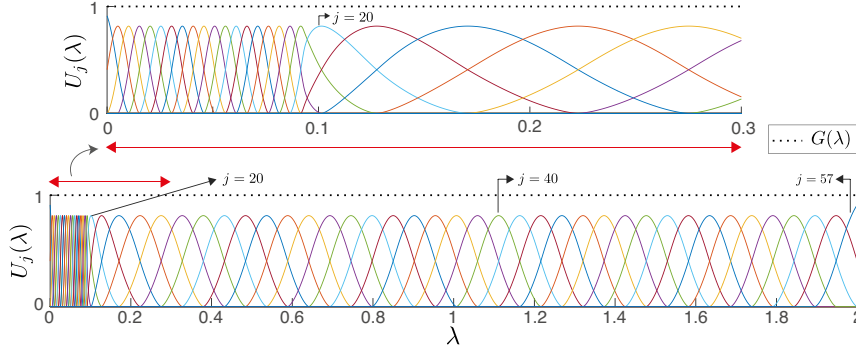


Figure 2. SOSKS57. The dotted lines correspond to $G(\lambda)$ in (20).

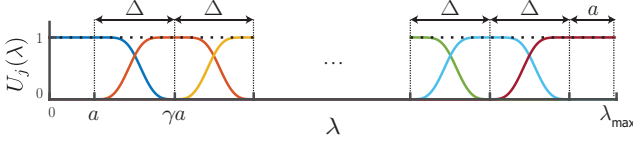


Figure 3. Construction of UMT system of spectral kernels.

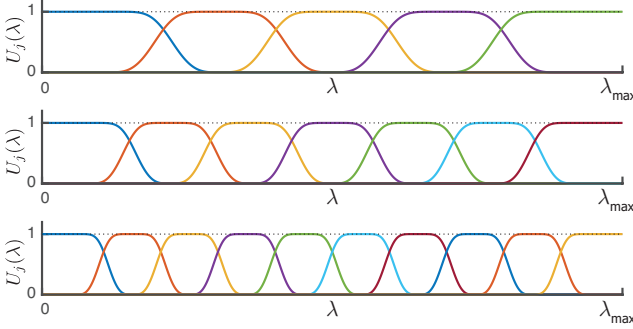


Figure 4. UMT system of spectral kernels with $J = 5$ (top), $J = 7$ (middle) and $J = 10$ (bottom) spectral scales. The dotted lines correspond to $G(\lambda)$ in (20).

Fig. 3 illustrates the notations used. By setting $\gamma = 2.73$, the set of kernels defined in (41) satisfies the uniformity constraint given in (55). The atoms of a dictionary constructed using this set of spectral kernels form a Parseval frame on $\ell_2(G)$.

Proof: See Appendix II. ■

Figs. 4(a) and (b) show realizations of the resulting UMT system of spectral kernels for a fixed λ_{\max} and two different J . The UMT system of spectral kernels have a narrow passband characteristic with the support of each kernel being a rather strict subset of the spectrum, with minimal overlap of adjacent kernels.

5. Ensemble Energy Spectral Density

The ensemble energy spectral density can be either computed using the graph Fourier transform or approximated through decomposition of the signals using polynomial approximation. In the former approach the ensemble energy is determined at the resolution of eigenvalues whereas in the latter approach it is determined at the resolution of a given number of subbands. The direct computation approach has two shortcomings. Firstly, it requires explicit computation of the graph spectrum and the associated eigenvectors; i.e., a full eigendecomposition

of the graph Laplacian matrix, which is computationally cumbersome for large graphs and infeasible for extensively large graphs. Secondly, it typically results in a non-smooth description of the ensemble energy. These shortcomings are resolved by using the polynomial approximation scheme.

5.A. Direct Computation: Using the Graph Fourier Transform

Definition (ensemble energy spectral density). For a given graph G , with spectrum $\Lambda(G)$, and graph signal set $F = \{\vec{f}_s\}_{s=1}^{N_s}$, the ensemble energy spectral density of F is obtained as

$$e_F[l] = \frac{1}{N_s} \sum_{s=1}^{N_s} |\hat{f}_s[l]|^2, \quad l = 1, \dots, N_g, \quad (43)$$

where \tilde{f}_s denotes the de-means and normalized version of f_s obtained as

$$\tilde{f}_s = \frac{\vec{f}_s - \sum_{r=1}^{1+m\lambda_1} \langle \vec{f}_s, \vec{\chi}_r \rangle \vec{\chi}_r}{\|\vec{f}_s - \sum_{r=1}^{1+m\lambda_1} \langle \vec{f}_s, \vec{\chi}_r \rangle \vec{\chi}_r\|_2}, \quad s = 1, \dots, N_s. \quad (44)$$

The ensemble energy spectral density has the following properties: (i) $\{e_F[r] = 0\}_{r=1}^{1+m\lambda_1}$, and (ii) $\sum_l e_F[l] = 1$.

5.A.1. Approximation: Using Decomposition through Polynomial Approximation.

The ensemble energy spectral density can be approximated through a multi subband decomposition scheme. Here we use the B-spline based system of spectral kernels, cf. A. The benefit in using a B-spline basis is in the smoothness characteristic of such kernels. Smooth overlapping kernels are advantageous it that i) they enable obtaining a smooth estimation of the ensemble energy spectral density and ii) they can be approximated as low order polynomials. We then decompose the graph signals using the designed system of kernels with a large number of subbands by exploiting the polynomial approximation scheme in decomposition. With such a decomposition, we approximate the ensemble spectral content of the signal set at the resolution of subbands.

Using a system of N_a B-spline based spectral kernels, $\{B_i(\lambda)\}_{i=1}^{N_a}$, the ensemble spectral energy of F can be

approximated at N_a overlapping bands across the spectrum as

$$a_F[i] = \frac{1}{N_s} \sum_{s=1}^{N_s} \sum_{n=1}^{N_g} \left| \langle \tilde{f}_s, \vec{\psi}_{B_i, n} \rangle \right|^2, \quad i = 1, \dots, N_a, \quad (45)$$

where \tilde{f}_s is as given in (44). Let $\vec{b}_j \in \ell_2(G)$ denote the discrete version of $B_j(\lambda)$, i.e.,

$$b_j[l] = B_j(\lambda_l), \quad l = 1, \dots, N_g. \quad (46)$$

We have $\sum_i a_F[i] = 1$ since

$$\sum_i a_F[i] \stackrel{(24)}{=} \frac{1}{N_s} \sum_{i=1}^{N_a} \sum_{s=1}^{N_s} \sum_{n=1}^{N_g} \left| \sum_{l=1}^{N_g} b_i[l] \hat{f}_s[l] \chi_l[n] \right|^2 \quad (47)$$

$$= \frac{1}{N_s} \sum_{s=1}^{N_s} \sum_{n=1}^{N_g} \left| \sum_{l=1}^{N_g} \underbrace{b_i^2[l]}_{\stackrel{(38)}{=} 1} \hat{f}_s[l] \chi_l[n] \right|^2 \quad (48)$$

$$= \frac{1}{N_s} \sum_{s=1}^{N_s} \sum_{n=1}^{N_g} \left| \sum_{l=1}^{N_g} \hat{f}_s[l] \chi_l[n] \right|^2 \quad (49)$$

$$\stackrel{(6)}{=} \frac{1}{N_s} \sum_{s=1}^{N_s} \sum_{n=1}^{N_g} |\tilde{f}_s[n]|^2 \quad (50)$$

$$= \frac{1}{N_s} \sum_{s=1}^{N_s} \|\tilde{f}_s\|_2^2 \quad (51)$$

$$\stackrel{(44)}{=} 1. \quad (52)$$

If desired, an explicit approximation of the ensemble energy spectral density of F , denoted $e_F^{(a)}[l]$, can also be determined. First, a continuous ensemble spectral energy representation, denoted $E_F^{(a)}(\lambda)$, is obtained through interpolating the set of points

$$\left\{ (0, 0) \cup \left\{ \left(\frac{\lambda_{\max}}{C} \sum_{k=1}^i \|B_k(\lambda)\|_2^2, a_F[i] \right) \right\}_{i=1}^{N_a} \right\}, \quad (53)$$

where $C = \sum_{k=1}^{N_a} \|B_k(\lambda)\|_2^2$. Then, $e_F^{(a)}[l]$ is obtained through sampling $E_F^{(a)}(\lambda)$ at $\Lambda(G)$ as

$$e_F^{(a)}[l] = E_F^{(a)}(\lambda_l), \quad l = 1, \dots, N_g. \quad (54)$$

6. Signal-Adapted System of Spectral Kernels

The construction of a signal-adapted system of spectral kernels is motivated by two observations: (i) the eigenvalues of the graph Laplacian that define the graph's spectrum are irregularly spaced, and depend in a complex way on the graph topology; (ii) the distribution of graph

signals' energy is generally non-uniform across the spectrum. Based on these observations, the idea is to construct an 'adapted' frame, such that the energy-wise significance of the eigenvalues is taken into account, rather than only adapting based on the distribution of the eigenvalues as proposed in (Shuman et al., 2015). In this way, also the topological information of the graph is implicitly incorporated in the design, since the energy content is given in the graph spectral domain that is in turn defined by the eigenvalues.

For the design of a signal-adapted system of spectral kernels with J subbands, denoted $\{S_j(\lambda)\}_{j=1}^J$, we start off from a prototype system of spectral kernels $\{U_j(\lambda)\}_{j=1}^J$ that satisfies the following two properties:

- (Uniformity constraint)

$$\exists C \in \mathbb{R}^+, \quad \int_0^{\lambda_{\max}} U_j(\lambda) d\lambda = C, \quad j = 1, \dots, J. \quad (55)$$

- (Tight Parseval frame constraint)

$$\sum_{j=1}^J |U_j(\lambda)|^2 = 1, \quad \forall \lambda \in [0, \lambda_{\max}]. \quad (56)$$

There is no unique system of kernels that satisfies (55) and (56). In this work we use the Meyer-like uniform system of spectral kernels (cf. B) that satisfies the two properties. We then use a suitable spectral-reorganisation transformation to warp the system of kernels to reorganise them along the spectrum to satisfy the desired signal adaptivity as entailed in the spectral-tuning transformation. Here we focus on one specific transform that aims to equalise the amount of ensemble energy that is captured by each kernel.

If the ensemble spectral density function is available, $T_F(\lambda)$ is obtained through monotonic cubic interpolation (Fritsch and Carlson, 1980) of the pair of points

$$\left\{ (0, 0) \cup \{(\lambda_l, \alpha_l)\}_{l=2}^{N_g-1} \cup (\lambda_{\max}, \lambda_{\max}) \right\}, \quad (57)$$

where Y_l is given as

$$\alpha_l = \frac{\lambda_{\max}}{m_{\lambda_l}} \sum_{r=i_{\lambda_l}}^{i_{\lambda_l} + m_{\lambda_l}} \sum_{k=1}^r e_F[k]. \quad (58)$$

If the ensemble energy spectral density is approximated using a system of N_a B-spline based spectral kernels, cf. (A.1), $T_F(\lambda)$ can instead be obtained through monotonic cubic interpolation of the set of points

$$\left\{ (0, 0) \cup \{(\omega_l, \alpha_l)\}_{l=1}^{N_a-1} \cup (\lambda_{\max}, \lambda_{\max}) \right\}, \quad (59)$$

where $C = \sum_{k=1}^{N_a} \|B_k(\lambda)\|_2^2$, and pairs (ω_l, α_l) are given

as

$$\omega_l = \frac{\lambda_{\max}}{C} \sum_{k=1}^i \|B_k(\lambda)\|_2^2 \quad (60)$$

$$\alpha_l = \lambda_{\max} \sum_{k=1}^i a_F[k]. \quad (61)$$

By incorporating a desired $T_F(\lambda)$ in $\{U_j(\lambda)\}_{j=1}^J$, a warped version of the prototype design is obtained as

$$S_j(\lambda) = U_j(T_F(\lambda)), \quad j = 1, \dots, J. \quad (62)$$

We refer to $\{S_j(\lambda)\}_{j=1}^J$ as a signal-adapted system of spectral kernels. The atoms of a dictionary constructed using $\{S_j(\lambda)\}_{j=1}^J$ form a Parseval frame on $\ell_2(G)$ since

$$\begin{aligned} \sum_{j=1}^J |S_j(\lambda)|^2 &\stackrel{(62)}{=} \sum_{j=1}^J |U_j(\underbrace{T_F(\lambda)}_{:=\lambda'})|^2, \quad \forall \lambda \in [0, \lambda_{\max}] \\ &= \sum_{j=1}^J |U_j(\lambda')|^2, \quad \forall \lambda' \in [0, \lambda_{\max}] \\ &= 1 \end{aligned}$$

where the last equality follows from Proposition 2. For direct decomposition as in (24), a discrete representation $\{s_j\}_{j=1}^J$ can be obtained through sampling $S_j(\lambda)$ at $\Lambda(G)$. With this design, each of the J spectral kernel $\{s_j\}_{j=1}^J$ capture an equal amount of ensemble energy. That is, if the ensemble energy spectral density is used we have

$$\sum_{l=1}^{N_g} s_j[l] e_F[l] \stackrel{(43)}{=} \frac{1}{J}, \quad j = 1, \dots, J, \quad (63)$$

and if the approximation scheme is used we have

$$\sum_{l=1}^{N_g} s_j[l] e_F^{(a)}[l] \stackrel{(54)}{=} \frac{1}{J}, \quad j = 1, \dots, J. \quad (64)$$

7. Example Designs and Applications of Signal-Adapted Decomposition of Graph Signals

We present constructions of signal-adapted systems of spectral kernels for signal sets realized on the Minnesota road graph, as well as three different brain graphs: template-based cerebellum gray matter graph (Behjat et al., 2015), individualised cerebral cortex graphs (Milloz et al., 2024), and individualised white matter graphs (Abramian et al., 2021).

7.A. The Minnesota Road Graph

The edges of the Minnesota Road Graph represent major roads and its vertices their intersection points, which often correspond to towns or cities, see Fig. 5(a). Fig. 5(b)

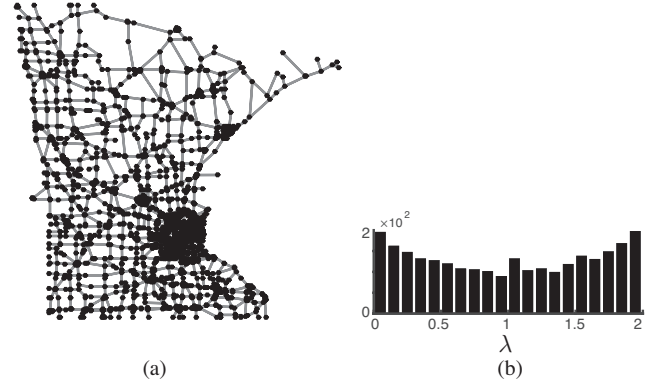


Figure 5. (a) Minnesota road graph. (b) Histograms of the eigenvalues $\Lambda_{\mathcal{L}}(G)$ of the Minnesota road graph. Each bar indicates the number of eigenvalues that lie in the corresponding spectral range.

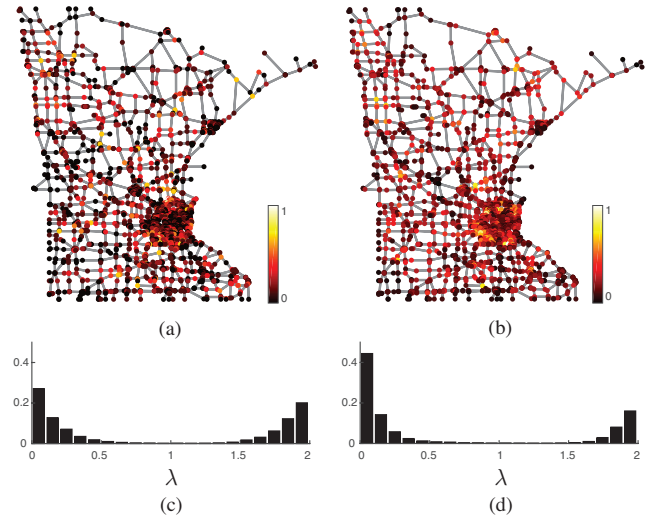


Figure 6. Sample signal realizations on the Minnesota road graph, (a) $\vec{x}_{0.2,2}$ and (b) $\vec{x}_{0.5,4}$. The plots are normalized as $\vec{x}_{\eta,n} / \|\vec{x}_{\eta,n}\|_{\infty}$ (c)-(d) Distribution of the ensemble energy spectral density e_{F1} and e_{F2} , respectively. Each bar indicates the sum of ensemble energies of the eigenvalues lying in the corresponding spectral range.

shows the graph's normalized Laplacian spectrum presented as the distribution of the eigenvalues.

Given the absence of real data for this commonly used benchmark graph, we consider a model for simulating random graph signals of varying smoothness. For a given graph with adjacency matrix A , a general model for realizing graph signals of density $\eta \in [0, 1]$ and smoothness $n \in \mathbb{Z}^+$ can be defined as

$$\vec{x}_{\eta,n} = A^n \vec{p}_{\eta}, \quad (65)$$

where $\vec{p}_{\eta} \in \ell_2(G)$ denotes a random realization of a spike signal as $\{\vec{p}_{\eta}[i]\}_{i=1, \dots, N_g}$ such that $\sum_i \vec{p}_{\eta}[i] = \eta N_g$. Application of the n -th power of A to \vec{p}_{η} leads to a signal that i) respects the intrinsic structure of the graph and ii) has a desired smoothness determined by n , a higher n leading to a smoother graph signal.

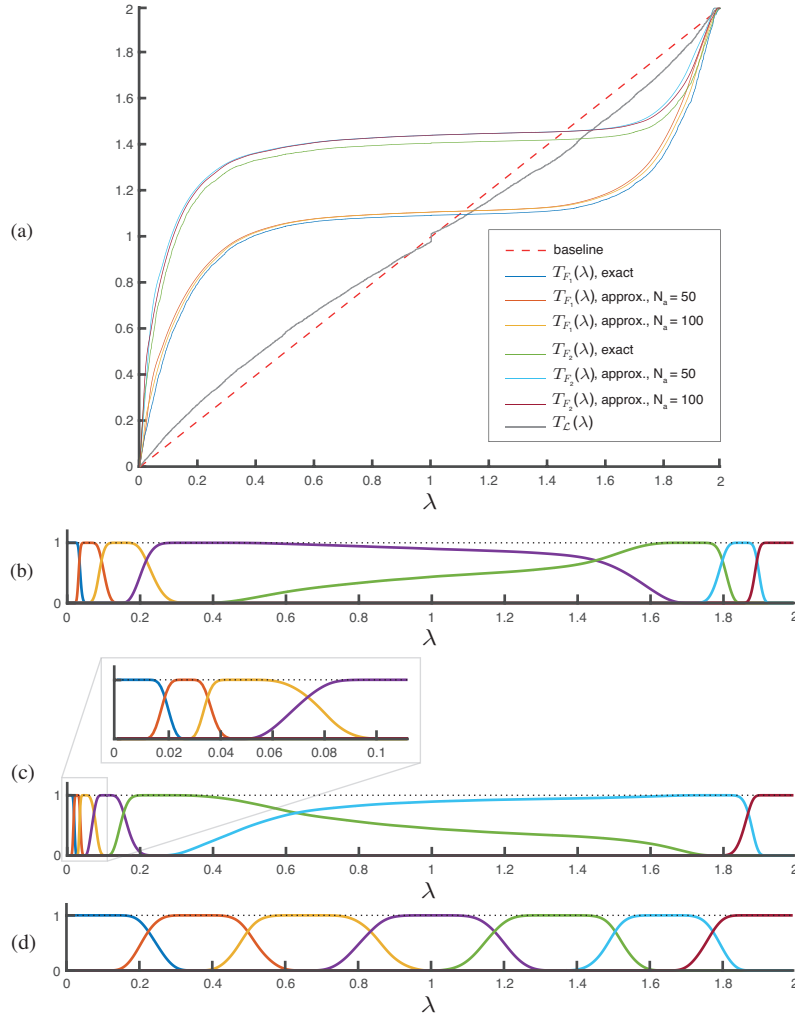


Figure 7. (a) Constructed energy-equalizing transformation functions, $T_{F_1}(\lambda)$ and $T_{F_2}(\lambda)$ using the exact and approximation schemes. N_a denotes the number of spectral kernels used for the approximation, cf. (54). (b)-(c) Signal-adapted system of spectral kernels constructed by warping the UMT system of spectral kernels ($J = 7$) using $T_{F_1}(\lambda)$ (approx., $N_a = 100$) and $T_{F_2}(\lambda)$ (approx., $N_a = 100$), respectively. (d) Spectrum-adapted system of spectral kernels constructed by warping the UMT system of spectral kernels ($J = 6$) using $T_{\mathcal{L}}(\lambda)$. In (b)-(d), the dotted lines corresponds to $G(\lambda)$ in (20).

Two sets of graph signals were constructed as

$$F_1 = \left\{ \left\{ \tilde{x}_{\eta,2}^{[i]} \right\}_{\eta=0.2,0.5} \right\}_{i=1,\dots,10},$$

$$F_2 = \left\{ \left\{ \tilde{x}_{\eta,4}^{[i]} \right\}_{\eta=0.2,0.5} \right\}_{i=1,\dots,10},$$

where index i denotes random realizations of p_η in (65), resulting in 20 signals in each set. Figs. 6(a) and (b) show a realizations of a signal from F_1 and F_2 , respectively.

Fig. 7(a) shows the energy-equalizing transformation functions associated to F_1 and F_2 . The transformations constructed based on a_{F_1} , cf. (59) closely matches that constructed based on e_{F_1} , cf. (57). The former transformation has the benefit of being smooth, and indeed, that it was computed without the explicit need to diagonalize L . By incorporating the transformations in the UMT system of spectral kernels, signal-adapted systems of spectral kernels are obtained, see Figs. 7(b)-(c).

A comparison of Figs. 7(b) and (c) and Figs. 6(c) and (d) highlights the energy-wise optimality of the proposed signal-adapted frame construction; i.e., more filters are

allocated to spectral ranges that have higher ensemble energy. The support of the filters in the two sets vary relative to the difference in the distribution of the ensemble energy of the two signal sets, with more filters allocated to the lower end of the spectrum for the F_2 frame than for the F_1 frame, and vice versa at the upper end of the spectrum. For comparison, a spectrum-adapted system of kernels is shown in Figs. 7(d). The spectrum-adapted system of kernels is obtained by warping the UMT prototype system of kernels with a spectrum-equalizing transformation function $T_{\mathcal{L}}(\lambda)$ which equalizes the distribution of the eigenvalues (Shuman et al., 2015). As the distribution of the eigenvalues of the Minnesota Road graph minimally deviate from a uniform distribution, so does the spectrum-adapted system of kernels relative to the UMT prototype, compare Figs. 4 and 7(d). On the contrary, the signal-adapted design optimizes the construction of the kernels such that the energy-wise significance of the eigenvalues is taken into account, rather than only considering the distribution of the eigenvalues as in the spectrum-adapted frame. Such adaptation results in a system of spectral kernels that largely deviate from the

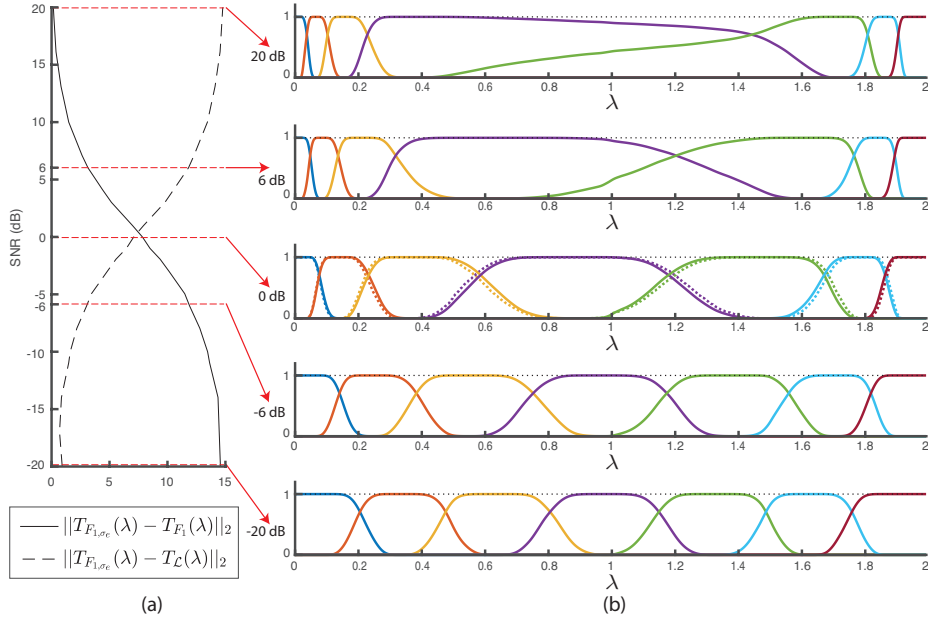


Figure 8. (a) Deviation of energy-equalizing transformation functions of noise added signal sets $T_{F_{1,\sigma_e}}(\lambda)$ relative to $T_{\mathcal{L}}(\lambda)$ and $T_{F_1}(\lambda)$ (cf. Fig. 7(a)) as a function of the signal sets' SNRs. (b) Signal-adapted system of spectral kernels constructed by warping the UMT system of spectral kernels ($J = 7$) using $T_{F_{1,\sigma_e}}(\lambda)$ of noise-added signal sets at five different SNRs. At 0 dB, the resulting system of kernels are overlaid on the system of kernels obtained by warping the UMT system of spectral kernels using the transformation function $(T_{F_1}(\lambda) + T_{\mathcal{L}}(\lambda))/2$, shown in dashed lines.

UMT prototype.

7.A.1. Robustness to Noise. It is interesting to study the robustness of the design to possible additive noise. Let F_{1,σ_e} denote the noise added version of signal set F_1 computed as

$$F_{1,\sigma_e} = \{\vec{y}_i = \vec{x}_i + \vec{e}_i \mid \vec{x}_i \in F_1\}_{i=1,\dots,20}, \quad (66)$$

where $\{\vec{e}_i\}_{i=1}^{20}$ denote random realizations of additive white Gaussian noise of standard deviation σ_e . We construct signal sets F_{1,σ_e} of varying $\text{SNR} = \sigma_x^2/\sigma_e^2$, where σ_x denotes the standard deviation of each signal $\vec{x}_i \in F_1$. Let $T_{F_{1,\sigma_e}}(\lambda)$ denote the energy-equalizing transformation function associated to F_{1,σ_e} . Fig. 8(a) shows mean-square error metrics $\|T_{F_{1,\sigma_e}}(\lambda) - T_{F_1}(\lambda)\|_2$ and $\|T_{F_{1,\sigma_e}}(\lambda) - T_{\mathcal{L}}(\lambda)\|_2$ across signal sets F_{1,σ_e} of varying SNR, where $T_{\mathcal{L}}(\lambda)$ and $T_{F_1}(\lambda)$ are the transformation functions shown in Fig. 7(a), $T_{F_1}(\lambda)$ being the approximated version using $N_a = 100$. The estimated energy-equalizing transformation functions $T_{F_{1,\sigma_e}}(\lambda)$ become more similar to $T_{F_1}(\lambda)$ as the SNR increases. At low SNRs, $T_{F_{1,\sigma_e}}(\lambda)$ become more similar to $T_{\mathcal{L}}(\lambda)$. The signal-adapted system of spectral kernels using noise-added signal sets of five different SNRs are shown in Fig. 8(b). At the two extremes, i.e., +20 dB and -20dB, the system of kernels become almost identical to the system of kernels shown in Figs. 7(b) and (d), respectively. At 0dB, the signal-adapted system of kernels at each subband can be seen as the average of the corresponding kernels in the associated subbands in Figs. 7(b) and (d). Equivalently, this can be seen as constructing a system of kernels through warping the the UMT prototype system of kernels with a warping function defined as the average of the spectrum-equalizing and energy-equalizing transfor-

mation functions, i.e., $(T_{F_1}(\lambda) + T_{\mathcal{L}}(\lambda))/2$, see Fig. 8(b) at 0 dB.

7.B. Multiscale Characterization of Brain Cortical Maps

GSP is highly effective in brain neuroimaging, with the objective to study and characterize brain anatomy, function, pathology, and their interactions. A common approach constructs a brain graph from anatomical features such as cortical morphology (from structural MRI) or white matter fiber architecture (from diffusion MRI). The brain's gray matter forms a convoluted structure interleaved with white matter and cerebrospinal fluid, while white matter consists of axonal fiber pathways. These structures enable detailed spatial modeling of individual brain anatomy as a graph.

Functional (e.g., functional MRI) and pathological (e.g., PET) neuroimaging data can be treated as graph signals, representing functions on a brain graph. Functional MRI (fMRI), a standard technique for studying brain function, captures blood-oxygen-level-dependent (BOLD) signals, which indicate changes in blood flow to active regions. Historically analyzed in gray matter (Logothetis and Wandell, 2004), recent studies have demonstrated its presence also in white matter (Li et al., 2019; Abramian et al., 2021; Schilling et al., 2023; Huang et al., 2023; Zu et al., 2024). In both tissues, the BOLD signal exhibits spatial patterns that are not well suited for analysis in a classical Euclidean framework, where filters and wavelets are typically isotropic and shift-invariant. Signal decompositions using Euclidean-based designs are thus inadequate for detecting non-isotropic BOLD signal in gray matter as well as elongated, low-amplitude BOLD signal that aligns with fiber bundles and crosses gray matter boundaries.

The same limitations hold for PET imaging data, specifically, PET-based manifestation of pathological proteins such as tau and amyloid-beta in Alzheimer's disease, which manifest notably heterogeneity in their spatial profiles that is linked to underlying anatomical boundaries. Anatomically adapted graph wavelets (Behjat et al., 2015) and low-pass filters tailored for white matter (Abramian et al., 2021; Behjat et al., 2025) have been proposed to address the need for designs that adapt to the domain of studied signals. However, challenges remain in designing flexible frames that suitably partition the spectrum for analysis of fMRI (Behjat and Larsson, 2020; Behjat et al., 2021; Ferritto et al., 2023). This motivates the need for a frame design that adapts to the spectral characteristics of fMRI and PET graph signals. Here we examine brain graph signal decompositions optimized for the energy distribution of fMRI and PET data, treated as graph signals on three types of anatomical brain graphs. In the first two applications (Sections B.1 and B.2), we use the design methodology introduced in Section 6 while in the third example (Section B.1) we show how a signal-adapted decomposition can be implemented more flexibly with user defined criteria.

7.B.1. Cerebellum graph and fMRI graph signals. We construct a graph encoding the 3D topology of cerebellar gray matter (Behjat et al., 2015) using an atlas-based template (Diedrichsen et al., 2009). Graph vertices represent gray matter voxels, while edges are defined by $3 \times 3 \times 3$ voxel neighborhood adjacency (Fig. 9). fMRI data were collected from 26 healthy subjects performing an event-related visual stimulation task (Kelly et al., 2008). Each subject underwent structural MRI and functional scans, which were co-registered and resampled to ensure voxel-wise alignment. Functional voxels corresponding to cerebellar gray matter were then extracted and treated as cerebellar graph signals. For each subject, a signal set $\{F_k\}_{k=1}^{26}$ was created by randomly selecting 20 functional signals. A combined signal set, $F = F_1 \cup F_2 \cup \dots \cup F_{26}$, was also constructed across all subjects.

Fig. 10(a) shows the distribution of the eigenvalues of the cerebellum graph. The distribution of the ensemble energy spectral density of signals sets F_1 , F_2 and F are shown in Figs. 10(b), (c) and (d), respectively. The distribution of eigenvalues is substantially different from that of the ensemble energy spectral densities; most eigenvalues are located at the upper end of the spectrum, whereas the ensemble energy is largely concentrated at the lower end of the spectrum. The ensemble energy spectral densities also vary across the signal sets. Sig-

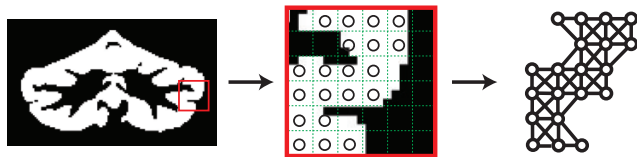


Figure 9. Illustration of the cerebellum graph.

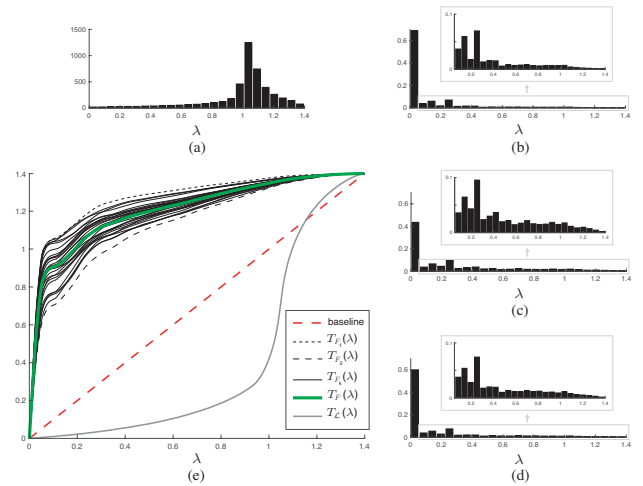


Figure 10. (a) Histogram of the eigenvalues $\Lambda_{\mathcal{L}}(G)$ of the cerebellum graph. (b)-(d) Distribution of the ensemble energy spectral density of F_1 , F_2 and F . (e) Energy-equalizing and spectrum-equalizing transformation functions. The black curves correspond to the energy-equalizing transformation for each subject's signal set. The upper and lower extreme transformations represented with dashed curves are associated to signal sets F_1 and F_2 , respectively.

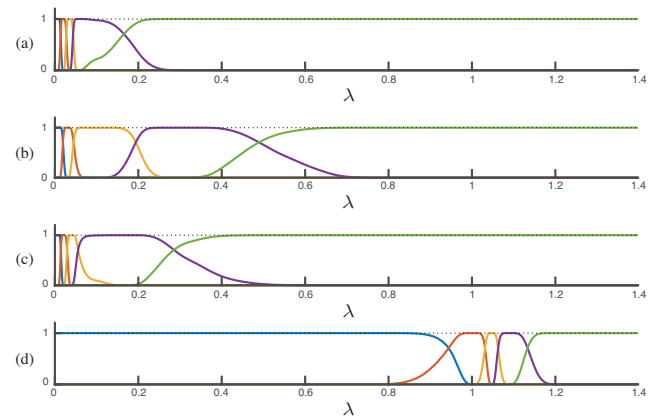


Figure 11. (a)-(c) Signal-adapted system of spectral kernels adapted to the ensemble spectral content of cerebellum graph signal sets F_1 , F_2 and F , respectively. (d) Spectrum-adapted system of spectral kernels.

nal set F_1 has more low energy spectral content than F_2 (compare the height of the first bins of the histograms in Figs. 10(b) and (c)), whereas F_2 shows greater spectral content at higher harmonics. F_1 and F_2 represent the two extremes across the subjects. The distribution of the ensemble energy content of F falls in between that of F_1 and F_2 , see Figs. 10(d). This is better observed by comparing the energy-equalizing transformation functions, see Fig. 10(e). The transformations associated to $\{F_k\}_{k=3}^{26}$ span the space in between $T_{F_1}(\lambda)$ and $T_{F_2}(\lambda)$, and $T_F(\lambda)$ falls almost in the mid range.

The stark contrast between eigenvalue and ensemble energy distributions results in a major discrepancy between $T_{\mathcal{L}}(\lambda)$ and the energy-equalizing transformations. Fig. 11 illustrates the resulting signal-adapted and spectrum-adapted systems of spectral kernels. The spectrum-adapted frame's kernels are concentrated at the higher end of the spectrum, where many eigenvalues lie, while signal-adapted frame kernels are localized at the lower end. This suggests that the signal-adapting scheme optimally configures filters based on

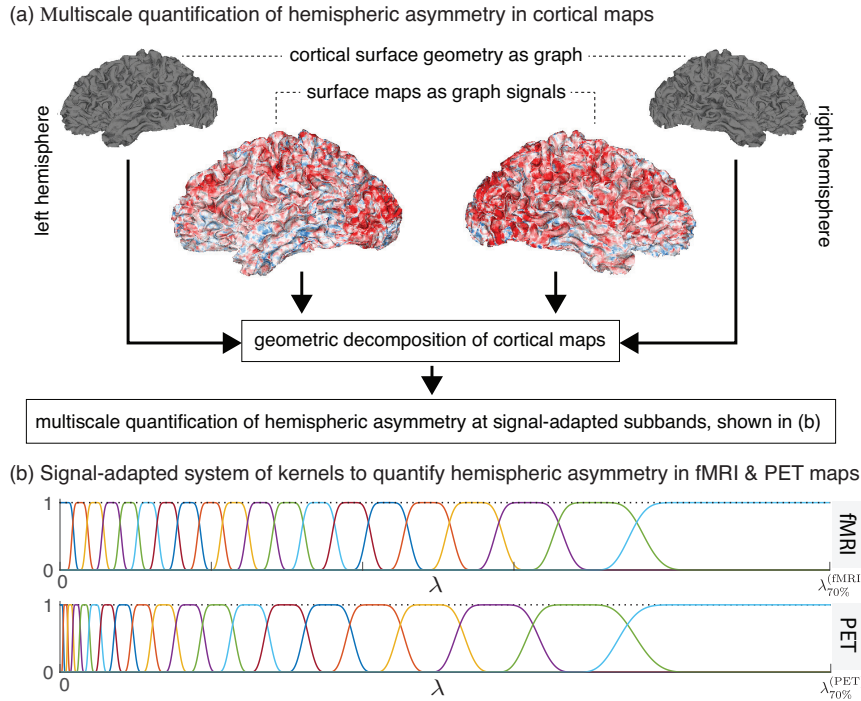


Figure 12. Signal-adapted, multiscale quantification of hemispheric asymmetry in brain cortical maps. (a) Schematic overview of the methodology. (b) Signal-adapted frames covering the lower-end of the spectrum up to the spectral value that on average 70% of the total ensemble spectral energy falls for fMRI (top) and tau-PET (bottom) cortical maps. Figure content based on (Milloz et al., 2024).

ensemble energy content. The proposed signal-adapted frame’s narrowband configuration at the lower spectrum end closely aligns with prior cerebellar data analysis methods (Behjat et al., 2015), which were empirically tuned using a Meyer-like graph wavelet frame (Leonardi and Van De Ville, 2013).

7.B.2. Cortical surface graph and fMRI/PET graph signals.

Hemispheric asymmetry is a fundamental feature of brain organization with implications for function, structure, and disease. Traditional methods for measuring hemispheric asymmetry rely on aggregate brain morphology metrics, such as surface area and gray matter volume, which capture only single spatial scales. For this type of analyses, the cortex is divided into atlas-defined regions, and laterality is determined by subtracting corresponding values in the left and right hemispheres. Cortical maps, however, exhibit both long- and short-range spatial frequency characteristics. Furthermore, the cerebral cortex is a continuous, highly convoluted structure that cannot be seamlessly partitioned into discrete regions at the individual level using non-invasive imaging.

Increasing evidence suggests that brain eigenmodes offer a powerful, generalized framework for studying the cortex’s multiscale structural (Cao et al., 2024; Maghsad-hagh et al., 2021; Mansour L et al., 2025; Wachinger et al., 2015) and functional organization (Behjat et al., 2025; Huang et al., 2018; Sina Mansour et al., 2024; Miri et al., 2024; Olsen et al., 2024; Tarun et al., 2020). A harmonic framework based on cortical surface eigenmodes can comprehensively capture spatial patterns and quantify lateralizations. Here, we apply the signal-adapted frame design methodology to define spatial subbands op-

timized for capturing lateralized spatial content in cortical fMRI and PET maps (Milloz et al., 2024) (Fig. 12(a)).

We study fMRI maps—from healthy young adults (Van Essen et al., 2013)—that represent each region’s functional connectivity, characterizing functional correlations/anti-correlations across the cortex. The PET maps—from cognitively unimpaired (CU) individuals and patients with Alzheimer’s disease (AD) dementia (Palmqvist et al., 2020)—quantify tau pathology, a key marker of AD dementia. We focus on the lower-end of the spectrum, capturing up to 70% of total signal energy in the studied maps, which corresponds to studying approximately the first 2000 eigenmodes when treating fMRI maps as graph signals and the first 500 when tau-PET maps are studied. This difference reflects the greater presence of larger spatial frequency content in fMRI connectivity maps compared to tau-PET maps. Fig.12(b) shows the resulting signal-adapted system of kernels, revealing subtle differences in subband configurations between the two datasets.

For the fMRI data, cortical regions in different canonical functional networks have connectivity patterns that manifest different degrees of hemispheric asymmetry in the different subbands (Fig. 13(a)). The results also reveal subject-specific idiosyncrasies in asymmetry across the different subbands and canonical networks. The greatest asymmetry is observed in the frontal, posterior parietal, and lateral temporal cortices.

For the tau-PET data, aggregates of the pathological tau protein manifest subtle asymmetries at varying spatial scales, which notably differs between CU individuals and patients with AD dementia (Fig. 13(b)). In both

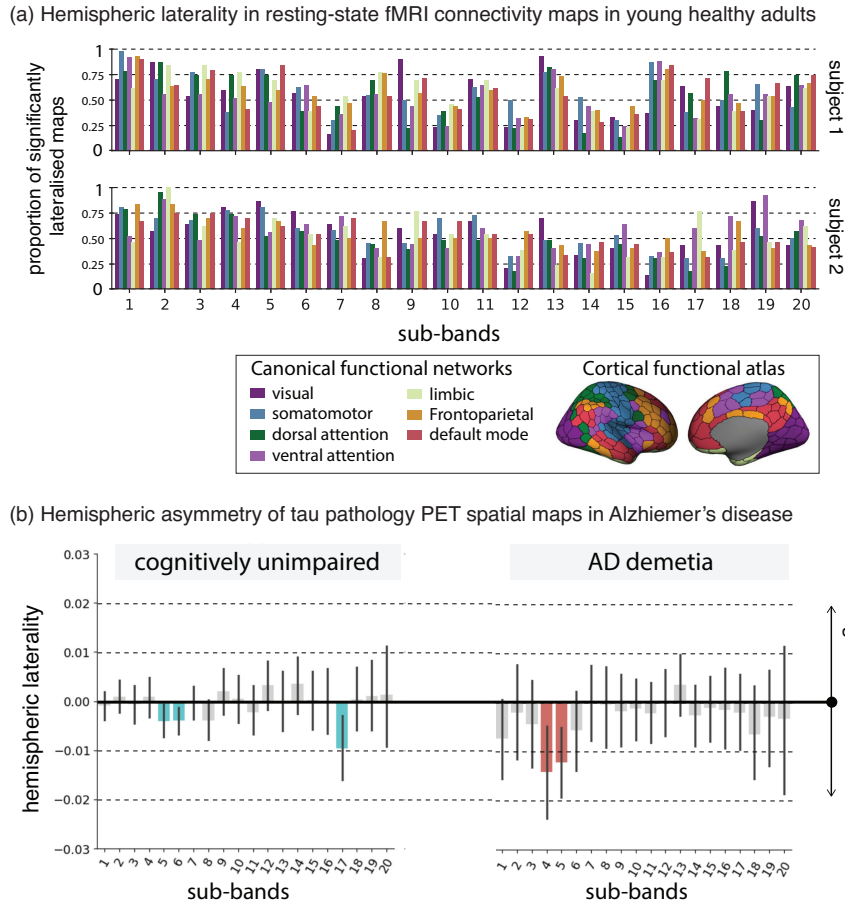


Figure 13. Signal-adapted quantification of hemispheric asymmetry in brain cortical maps. (a) Proportion of fMRI seed connectivity maps that manifest significant laterality in the different spectral bands. Results shown for two representative subjects. (d) Hemispheric asymmetry in tau-PET maps in cognitively unimpaired patients and in patients with AD dementia. Figure content based on (Milloz et al., 2024).

groups, significant leftward asymmetry is observed in several subbands (highlighted subbands), with the laterality being substantially larger in the patients with AD dementia in the geometric spatial scale that is represented by the fourth and fifth signal-adapted subbands.

7.B.3. White matter graph and fMRI graph signals. To demonstrate the flexibility of signal-adapted graph signal decompositions, in this final application we employ a decomposition without the explicit use of the “warping procedure” described under Section 6, i.e., Eq. (62). However, it still utilizes ensemble spectral energy estimates to guide the construction of spectral kernels tailored to the spectral characteristics of the signals at hand.

We construct individualized graphs encoding white matter fiber architecture using diffusion MRI data (Abramian et al., 2021), as shown in Fig. 14(a). For each subject (95 total) and hemisphere, a graph is built where white matter voxels serve as vertices. Edges between adjacent voxels are weighted based on the coherence of their diffusion orientation distribution functions (ODFs)—higher weights indicate better alignment with the connecting edge. We refer the interested reader to (Abramian et al., 2021) for further design details.

Fig. 14(b) illustrates the spectral energy distribution of white matter fMRI graph signals across subjects, esti-

mated using the multi-resolution spectral kernel system (Fig. 2) via polynomial approximation (cf. Section A.1). Over 50% of total spectral energy is concentrated in eigenvectors with eigenvalues in $[0, 0.1]$, while less than 1% is in $[1.4, 2]$. Overall, more than 90% of ensemble signal energy is captured by eigenvectors in the lower half of the spectrum. Given this distribution of energies, and in order to reduce the dimensionality of the spectral representation, we studied variations in the spectral energy of white matter fMRI maps using a coarser set of five spectral kernels as shown at the bottom of Fig. 14(b). This system of kernels, which form a Parseval frame, was defined by merging the narrowband kernels of the system of kernels (i.e. Fig. 2) used to estimate the energy content: the first kernel covers the lower 5% of the spectrum (first 20 kernels of Fig. 2, as in prior studies (Behjat and Larsson, 2020)), the last spans the upper-end of the spectrum the eigenmode of which capture 1% of total signal energy, and the remainder of the spectrum is divided into three bands, each capturing roughly an equal amount of the total spectral energy.

Fig. 14(c) compares changes in ensemble spectral energy across the five defined bands during an fMRI task. SE in band 1 decreases over time, while bands 2-4 show an overall increase, and band 5 remains largely unchanged. Notably, spectral content shifts significantly

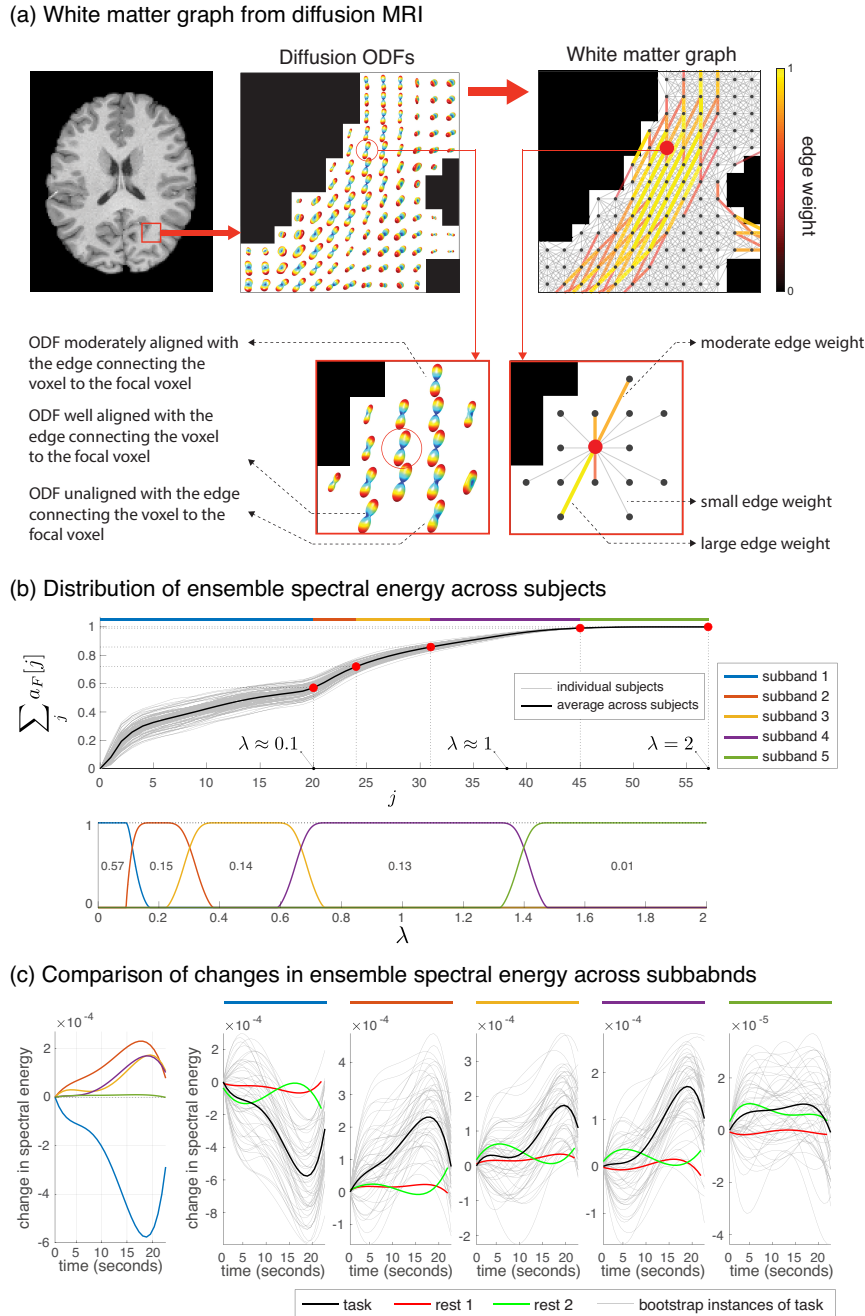


Figure 14. Signal-adapted decomposition of fMRI data in white matter. (a) A schematic illustration of the white matter graph of a representative subject. (b) Ensemble spectral energy estimates using the system of kernels shown in Fig. 2 across 95 subjects. A five-band system of spectral kernels is defined based on these estimates. The first kernel covers the lower 5% of the spectrum, the last spans the region capturing 1% of total signal energy, and the remainder of the spectrum is divided into three bands, each capturing roughly equal amount of total ensemble signal energy; values shown in the kernels are fraction of total ensemble captured per band. (c) Figure content based on (Abramian et al., 2021; Behjat et al., 2021).

10 seconds post-stimulus, potentially reflecting delayed hemodynamic response peaks in white matter, observed in multiple WM fiber bundles at a similar delay (Li et al., 2019).

8. Conclusion & Outlook

We presented a scheme for designing signal-adapted frames on graphs, leveraging the ensemble energy spectral density of a given signal set. The design, based solely on stationary signal information, allows flexibility in capturing non-stationary features through adjustable

bandpass characteristics. While formulated on the graph Laplacian spectrum, the design can be extended to the spectrum of other graph shift operators, e.g. the graph adjacency spectrum to enable signal-adapted decomposition on directed graphs (Sevi et al., 2023; Chan et al., 2024; Stanković et al., 2025), or even to that of high-order networks (Schaub et al., 2021; Santoro et al., 2023; Dal Col et al., 2024). The proposed methods may also be used to design efficient graph filters for use in graph convolutional layers (Defferrard et al., 2016; Dong et al., 2020; Liu et al., 2024).

Acknowledgements

This work draws in part on material previously published in (Abramian et al., 2021; Behjat et al., 2021, 2016; Milloz et al., 2024).

Appendix 1 - Proof of Proposition 1

The sum of squared magnitudes of B-spline based spectral kernels $\{B_j(\lambda)\}_{j=1}^J$ forms a partition of unity since

$$\begin{aligned} \sum_{j=1}^J |B_j(\lambda)|^2 &\stackrel{(36)}{=} \sum_{i=\Delta}^{J+\Delta+1} |\tilde{B}_i(\lambda)|^2 \\ &\stackrel{(37)}{=} \sum_{i=\Delta}^{J+\Delta+1} \beta^{(n)} \left(\frac{\lambda_{\max}}{J-1} (\lambda - i + 1) \right) \\ &\stackrel{i-1 \rightarrow k}{=} \sum_{k=\Delta-1}^{J+\Delta} \beta^{(n)} \left(\frac{\lambda_{\max}}{J-1} (\lambda - k) \right) \\ &= 1. \end{aligned}$$

where in the last equality we use the property that integer shifted splines form a partition of unity.

Appendix 2 - Proof of Proposition 2

In order to ensure that the spectral kernels cover the full spectrum, a must be chosen such that

$$\lambda_{\max} \stackrel{(41c)}{=} \lambda_{\parallel} + a \stackrel{(j=J)}{=} \gamma a + (J-2)\Delta + a,$$

which using (42a) leads to $a = \frac{\lambda_{\max}}{J\gamma - J - \gamma + 3}$.

To prove that the UMT system of spectral kernels form a tight frame, (21) needs to be fulfilled. Since, for all j , the supports of $U_{j-1}(\lambda)$ and $U_{j+1}(\lambda)$ are disjoint, $G(\lambda)$ can be determined as

$$\begin{aligned} G(\lambda) &= \sum_{j=1}^J |U_j(\lambda)|^2 \\ &\stackrel{(41)}{=} \begin{cases} |U_1(\lambda)|^2 \stackrel{(41a)}{=} 1 & \forall \lambda \in [0, a] \\ |U_1(\lambda)|^2 + |U_2(\lambda)|^2 & \forall \lambda \in]a, \gamma a] \\ |U_2(\lambda)|^2 + |U_3(\lambda)|^2 & \forall \lambda \in]\gamma a, \gamma a + \Delta] \\ \vdots & \vdots \\ |U_J(\lambda)|^2 \stackrel{(41c)}{=} 1 & \forall \lambda \in]\lambda_{\max} - a, \lambda_{\max}] \end{cases} \\ &\stackrel{(41b)}{=} \begin{cases} 1 & \forall \lambda \in [0, a] \\ \cos^2(x_{\parallel}) + \sin^2(x_{\parallel}) & \forall \lambda \in]a, \gamma a] \\ \cos^2(x_{\parallel}) + \sin^2(x_{\parallel}) & \forall \lambda \in]\gamma a, \gamma a + \Delta] \\ \vdots & \vdots \\ 1 & \forall \lambda \in]\lambda_{\max} - a, \lambda_{\max}] \end{cases} \\ &= 1 \quad \forall \lambda \in [0, \lambda_{\max}] \end{aligned} \quad (67)$$

where $x_{\parallel} = \frac{\pi}{2} \nu \left(\frac{1}{\gamma-1} \left(\frac{\lambda}{a} - 1 \right) \right)$ and $x_{\perp} = \frac{\pi}{2} \nu \left(\frac{1}{\gamma-1} \left(\frac{\lambda - \Delta}{a} - 1 \right) \right)$.

For any given γ , the constructed set of spectral kernels form a tight frame. However, in order for the frame to satisfy the uniformity constraint given in (55), the appropriate γ needs to be determined. From (41b), we have $\forall j \in \{2, \dots, J-2\}$

$$U_j(\lambda) = U_{j+1}(\lambda + \Delta) \quad \forall \lambda \in]\lambda_{\parallel}, \lambda_{\parallel} + \Delta]. \quad (68)$$

By considering an inverse linear mapping of the spectral support where $U_1(\lambda) \neq 0$, i.e. $[0, \gamma a]$, to the spectral support where $U_J(\lambda) \neq 0$, i.e. $[\lambda_{\max} - \gamma a, \lambda_{\max}]$, we have

$$U_1(\lambda) = U_J(-\lambda + 2a + J\Delta) \quad \forall \lambda \in [0, \gamma a]. \quad (69)$$

Thus, from (68) and (69) we have

$$\int_0^{\lambda_{\max}} U_j(\lambda) d\lambda = C_2, \quad j = 2, \dots, J-1 \quad (70a)$$

$$\int_0^{\lambda_{\max}} U_1(\lambda) d\lambda = \int_0^{\lambda_{\max}} U_J(\lambda) d\lambda = C_1, \quad (70b)$$

respectively, where $C_1, C_2 \in \mathbb{R}^+$. Thus, in order to satisfy (55), γ should be chosen such that

$$\begin{aligned} C_1 &= C_2 \\ \int_0^{\lambda_{\max}} U_1(\lambda) d\lambda &= \int_0^{\lambda_{\max}} U_2(\lambda) d\lambda \\ a + \int_a^{\gamma a} U_1(\lambda) d\lambda &= \int_a^{\gamma a} \sin\left(\frac{\pi}{2} \nu\left(\frac{1}{\gamma-1}\left(\frac{\lambda}{a} - 1\right)\right)\right) d\lambda \\ &\quad + \int_{\gamma a}^{\gamma a + \Delta} U_2(\lambda) d\lambda \\ &\stackrel{(68)}{=} \int_a^{\gamma a} \sin\left(\frac{\pi}{2} \nu\left(\frac{1}{\gamma-1}\left(\frac{\lambda}{a} - 1\right)\right)\right) d\lambda. \end{aligned} \quad (71)$$

The optimal γ that satisfies (71) was obtained numerically by defining

$$Q(\gamma) = \int_a^{\gamma a} \sin\left(\frac{\pi}{2} \nu\left(\frac{1}{\gamma-1}\left(\frac{\lambda}{a} - 1\right)\right)\right) d\lambda - a, \quad (72)$$

and discretizing $Q(\gamma)$ within the range $(a, \gamma a]$, with a sampling factor of 1×10^{-4} . Testing for $\gamma \geq 1$, with a step size of 1×10^{-2} , the optimal value, which is independent of λ_{\max} and J , was found to be $\gamma = 2.73$.

References

- Abramian, D., Larsson, M., Eklund, A., Aganj, I., Westin, C.-F., and Behjat, H. Diffusion-informed spatial smoothing of fMRI data in white matter using spectral graph filters. *NeuroImage*, 237:118095, 2021.
- Behjat, H. and Larsson, M. Spectral characterization of functional MRI data on voxel-resolution cortical graphs. In *Proc. IEEE Int. Symp. Biomed. Imaging*, pages 558–562, 2020.
- Behjat, H., Leonardi, N., Sörnmo, L., and Van De Ville, D. Anatomically-adapted graph wavelets for improved group-level fMRI activation mapping. *NeuroImage*, 123:185–199, 2015.
- Behjat, H., Richter, U., Van De Ville, D., and Sörnmo, L. Signal-adapted tight frames on graphs. *IEEE Trans. Signal Process.*, 64(22):6017–6029, 2016.
- Behjat, H., Westin, C.-F., and Aganj, I. Cortical surface-informed volumetric spatial smoothing of fMRI data via graph signal processing. In *Proc. IEEE Int. Conf. Eng. Med. Biol. Soc.*, pages 3804–3808. IEEE, 2021.

- Behjat, H., Aganj, I., Abramian, D., Eklund, A., and Westin, C.-F. Characterization of spatial dynamics of fMRI data in white matter using diffusion-informed white matter harmonics. In *Proc. IEEE Int. Symp. Biomed. Imaging*, pages 1586–1590. IEEE, 2021.
- Behjat, H., Tarun, A., Abramian, D., Larsson, M., and Van De Ville, D. Voxel-Wise Brain Graphs From Diffusion MRI: Intrinsic Eigenspace Dimensionality and Application to Functional MRI. *IEEE Open Journal of Engineering in Medicine and Biology*, 6:158–167, 2025.
- Benedetto, J. and Fickus, M. Finite normalized tight frames. *Adv. Comput. Math.*, 18(2):357–385, 2003.
- Cao, T., Pang, J. C., Segal, A., Chen, Y.-C., Aquino, K. M., Breakpear, M., and Fornito, A. Mode-based morphometry: A multiscale approach to mapping human neuroanatomy. *Human Brain Mapping*, 45(4):e26640, 2024.
- Chan, C. H. M., Cionca, A., and Van De Ville, D. Hilbert Transform on Graphs: Let There Be Phase. *arXiv preprint arXiv:2412.18501*, 2024.
- Chung, F. *Spectral graph theory*. AMS, Providence, RI, 1997.
- Coifman, R. R. and Maggioni, M. Diffusion wavelets. *Appl. Comput. Harmon. Anal.*, 21(1):53–94, 2006.
- Dal Col, A., Petronetto, F., de Oliveira Neto, J. R., and Lima, J. B. Windowed hypergraph fourier transform and vertex-frequency representation. *Signal Processing*, 223:109538, 2024.
- Defferrard, M., Bresson, X., and Vandergheynst, P. Convolutional neural networks on graphs with fast localized spectral filtering. *Advances in neural information processing systems*, 29, 2016.
- Diedrichsen, J., Balsters, J. H., Flavell, J., Cussans, E., and Ramnani, N. A probabilistic MR atlas of the human cerebellum. *Neuroimage*, 46(1):39–46, 2009.
- Dong, X., Thanou, D., Toni, L., Bronstein, M., and Frossard, P. Graph signal processing for machine learning: A review and new perspectives. *IEEE Signal processing magazine*, 37(6):117–127, 2020.
- Ferritto, C., Preti, M. G., Moia, S., Van De Ville, D., and Behjat, H. Brain fingerprinting using fMRI spectral signatures on high-resolution cortical graphs. In *Proc. IEEE Int. Conf. Acoust. Speech and Signal Process. Workshops*, pages 1–5. IEEE, 2023.
- Fiedler, M. Algebraic connectivity of graphs. *Czechoslov. Math. J.*, 23(2):298–305, 1973.
- Fritsch, F. N. and Carlson, R. E. Monotone piecewise cubic interpolation. *SIAM J. Numer. Anal.*, 17(2):238–246, 1980.
- Gavish, M., Nadler, B., and Coifman, R. R. Multiscale wavelets on trees, graphs and high dimensional data: Theory and applications to semi supervised learning. In *Proc. Int. Conf. Mach. Learn.*, pages 367–374, 2010.
- Ghandehari, M., Guillot, D., and Hollingsworth, K. Gabor-type frames for signal processing on graphs. *Journal of Fourier Analysis and Applications*, 27:1–23, 2021.
- Ghandehari, M., Janssen, J., and Kalyaniwalla, N. A noncommutative approach to the graphon Fourier transform. *Applied and Computational Harmonic Analysis*, 61:101–131, 2022.
- Girvan, M. and Newman, M. E. Community structure in social and biological networks. *Proc. Natl Acad. Sci.*, 99(12):7821–7826, 2002.
- Hammond, D., Vandergheynst, P., and Gribonval, R. Wavelets on graphs via spectral graph theory. *Appl. Comput. Harmon. Anal.*, 30(2):129–150, 2011.
- Huang, W., Bolton, T. A. W., Medaglia, J. D., Bassett, D. S., Ribeiro, A., and Ville, D. V. A graph signal processing perspective on functional brain imaging. *Proceedings of the IEEE*, 106(5):868–885, May 2018. doi: 10.1109/JPROC.2018.2798928.
- Huang, Y., Wei, P.-H., Xu, L., Chen, D., Yang, Y., Song, W., Yi, Y., Jia, X., Wu, G., Fan, Q., et al. Intracranial electrophysiological and structural basis of BOLD functional connectivity in human brain white matter. *Nat Commun*, 14(1):3414, 2023.
- Isufi, E., Gama, F., Shuman, D. I., and Segarra, S. Graph filters for signal processing and machine learning on graphs. *IEEE Transactions on Signal Processing*, 2024.
- Jansen, M., Nason, G. P., and Silverman, B. W. Multiscale methods for data on graphs and irregular multidimensional situations. *J. Roy. Statistical Soc.: Series B (Statistical Methodology)*, 71(1):97–125, 2009.
- Kelly, A. M. C., Uddin, L. Q., Biswal, B. B., Castellanos, F. X., and Milham, M. P. Competition between functional brain networks mediates behavioral variability. *Neuroimage*, 39(1):527–537, 2008.
- Leonardi, N. and Van De Ville, D. Tight wavelet frames on multislice graphs. *IEEE Trans. Signal Process.*, 61(13):3357–3367, 2013.
- Li, M., Newton, A. T., Anderson, A. W., Ding, Z., and Gore, J. C. Characterization of the hemodynamic response function in white matter tracts for event-related fMRI. *Nat. Commun.*, 10(1):1–11, 2019.
- Liu, N., He, X., Laurent, T., Di Giovanni, F., Bronstein, M. M., and Bresson, X. Advancing graph convolutional networks via general spectral wavelets. *arXiv preprint arXiv:2405.13806*, 2024.
- Logothetis, N. and Wandell, B. Interpreting the BOLD signal. *Annu. Rev. Physiol.*, 66:735–769, 2004.
- Maghsadghagh, S., da Rocha, J. L. D., Benner, J., Schneider, P., Golestani, N., and Behjat, H. A discriminative characterization of Heschl’s gyrus morphology using spectral graph features. In *2021 43rd Annual International Conference of the IEEE Engineering in Medicine & Biology Society (EMBC)*, pages 3577–3581. IEEE, 2021.
- Mansour L, S., Di Biase, M. A., Yan, H., Xue, A., Venketasubramanian, N., Chong, E., Alexander-Bloch, A., Chen, C., Zhou, J. H., Yeo, B. T., et al. Spectral normative modeling of brain structure. *medRxiv*, pages 2025–01, 2025.
- Meyer, Y. Principe d’incertitude, bases hilbertiennes et algebres d’operateurs. *Seminaire Bourbaki (in French)*, 662:209–223, 1986.
- Milloz, A., Vogel, J., Olsen, A., Pang, J. C., Strandberg, O., Anijã? rv, T. E., Stomrud, E., Palmqvist, S., Spotorno, N., Ossenkoppelle, R., et al. Multiscale quantification of hemispheric asymmetry in cortical maps using geometric eigenmodes. *bioRxiv*, pages 2024–10, 2024.
- Miri, M., Abootelebi, V., Saeedi-Sourck, H., Van De Ville, D., and Behjat, H. Spectral representation of EEG data using learned graphs with application to motor imagery decoding. *Biomedical Signal Processing and Control*, 87:105537, 2024.
- Narang, S. K. and Ortega, A. Lifting based wavelet transforms on graphs. In *Proc. APSIPA ASC*, pages pp. 441–444, 2009.
- Narang, S. K. and Ortega, A. Perfect reconstruction two-channel wavelet filter banks for graph structured data. *IEEE Trans. Signal Process.*, 60(6):2786–2799, 2012.
- Newman, M. *Networks*. OUP Oxford, Mar. 2010.
- Olsen, A. S., Mansour L, S., Pang, J. C., Zalesky, A., Van De Ville, D., and Behjat, H. On reconstruction of cortical functional maps using subject-specific geometric and connectome eigenmodes. *bioRxiv*, pages 2024–10, 2024.
- Ortega, A., Frossard, P., Kovačević, J., Moura, J. M. F., and Vandergheynst, P. On the optimality of ideal filters for pyramid and wavelet signal approximation. *Proc. IEEE*, 106(5):808–828, 2018.
- Palmqvist, S., Janelidze, S., Quiroz, Y. T., Zetterberg, H., Lopera, F., Stomrud, E., Su, Y., Chen, Y., Serrano, G. E., Leuzy, A., et al. Discriminative accuracy of plasma phospho-tau217 for Alzheimer disease vs other neurodegenerative disorders. *Jama*, 324(8):772–781, 2020.
- Ram, I., Elad, M., and Cohen, I. Redundant wavelets on graphs and high dimensional data clouds. *IEEE Signal Process. Lett.*, 19(5): 291–294, 2012.
- Sandryhaila, A. and Moura, J. Discrete signal processing on graphs. *IEEE Trans. Signal Process.*, 61:1644–1656, 2013.
- Santoro, A., Battiston, F., Petri, G., and Amico, E. Higher-order organization of multivariate time series. *Nature Physics*, 19(2):221–229, 2023.
- Schaub, M. T., Zhu, Y., Seby, J.-B., Roddenberry, T. M., and Segarra, S. Signal processing on higher-order networks: Livin’ on the edge... and beyond. *Signal Processing*, 187:108149, 2021.
- Schilling, K. G., Li, M., Rheault, F., Gao, Y., Cai, L., Zhao, Y., Xu, L., Ding, Z., Anderson, A. W., Landman, B. A., et al. Whole-brain, gray, and white matter time-locked functional signal changes with simple tasks and model-free analysis. *Proc. Natl Acad. Sci.*, 120(42):e2219666120, 2023.
- Sevi, H., Rilling, G., and Borgnat, P. Harmonic analysis on directed graphs and applications: From Fourier analysis to wavelets. *Applied and Computational Harmonic Analysis*, 62:390–440, 2023.
- Shuman, D. I., Narang, S. K., Frossard, P., Ortega, A., and Vandergheynst, P. The emerging field of signal processing on graphs: Extending high-dimensional data analysis to networks and other irregular domains. *IEEE Signal Process. Mag.*, 30(3):83–98, 2013.
- Shuman, D. I., Ricaud, B., and Vandergheynst, P. Vertex-frequency analysis on graphs. *Appl. Comput. Harmon. Anal.*, 2015. doi: 10.1016/j.acha.2015.02.005.
- Shuman, D. I., Wiesmeyer, C., Holighaus, N., and Vandergheynst, P. Spectrum-adapted tight graph wavelet and vertex-frequency frames. *IEEE Trans. Signal Process.*, 63(16):4223–4235, 2015.
- Shuman, D. I., Faraji, M. J., and Vandergheynst, P. A multiscale pyramid transform for graph signals. *IEEE Trans. Signal Process.*, 64(8): 2119–2134, 2016.
- Shuman, D. I. Localized spectral graph filter frames: A unifying framework, survey of design considerations, and numerical comparison.

- IEEE Signal Processing Magazine*, 37(6):43–63, 2020.
- Sina Mansour, L., Behjat, H., De Ville, D. V., Smith, R. E., Yeo, B. T., and Zalesky, A. Eigenmodes of the brain: revisiting connectomics and geometry. *bioRxiv*, pages 2024–04, 2024.
- Stankovic, L., Dakovic, M., and Sejdic, E. Vertex-frequency analysis: A way to localize graph spectral components [lecture notes]. *IEEE Signal Process. Mag.*, 34(4):176–182, 2017.
- Stankovic, L., Mandic, D. P., Dakovic, M., Kisil, I., Sejdic, E., and Constantinides, A. G. Understanding the basis of graph signal processing via an intuitive example-driven approach [lecture notes]. *IEEE Signal Processing Magazine*, 36(6):133–145, 2019.
- Stanković, L., Mandic, D., Daković, M., Scalzo, B., Brajović, M., Sejdčić, E., and Constantinides, A. G. Vertex-frequency graph signal processing: A comprehensive review. *Digital signal processing*, 107: 102802, 2020.
- Stanković, L., Daković, M., Bardi, A. B., Brajović, M., and Stanković, I. Fourier analysis of signals on directed acyclic graphs (dag) using graph zero-padding. *Digital Signal Processing*, page 104995, 2025.
- Tanaka, Y. and Sakiyama, A. M-channel oversampled graph filter banks. *IEEE Trans. Signal Process.*, 62(14):3578–3590, 2014.
- Tarun, A., Behjat, H., Bolton, T., Abramian, D., and Van De Ville, D. Structural mediation of human brain activity revealed by white-matter interpolation of fMRI. *Neuroimage*, 213:116718, 2020.
- Thanou, D., Shuman, D. I., and Frossard, P. Learning parametric dictionaries for signals on graphs. *IEEE Trans. Signal Process.*, 62(15): 3849–3862, 2014.
- Tremblay, N. and Borgnat, P. Subgraph-based filterbanks for graph signals. *IEEE Trans. Signal Process.*, 64(15):3827–3840, 2016.
- Van De Ville, D., Demesmaeker, R., and Preti, M. G. When slepian meets fiedler: Putting a focus on the graph spectrum. *IEEE Signal Process. Lett.*, 24(7):1001–1004, 2017.
- Van Essen, D., Smith, S., Barch, D., Behrens, T., Yacoub, E., Ugurbil, K., and Consortium., W.-M. H. The WU-Minn human connectome project: an overview. *Neuroimage*, 80:62–79, 2013.
- Von Luxburg, U. A tutorial on spectral clustering. *Stat. Comput.*, 17(4): 395–416, 2007.
- Wachinger, C., Golland, P., Kremen, W., Fischl, B., Reuter, M., Initiative, A. D. N., et al. Brainprint: a discriminative characterization of brain morphology. *Neuroimage*, 109:232–248, 2015.
- Yankelevsky, Y. and Elad, M. Dual graph regularized dictionary learning. *IEEE Trans. Signal Info. Process. Netw.*, 2(4):611–624, 2016.
- Zhao, R. and Tay, D. B. Minimax design of two-channel critically sampled graph QMF banks. *Signal Processing*, 212:109129, 2023.
- Zu, Z., Choi, S., Zhao, Y., Gao, Y., Li, M., Schilling, K. G., Ding, Z., and Gore, J. C. The missing third dimension—Functional correlations of BOLD signals incorporating white matter. *Sci Adv*, 10(4):eadi0616, 2024.